Energy & Environmental Science

ARTICLE

High-rate in-plane micro-supercapacitors scribed onto photo paper using *in-situ* femtolaser-reduced graphene oxide/Au nanoparticle microelectrodes

fReceived 00th January 20xx,
Accepted 00th January 20xx

DOI: 10.1039/x0xx00000x

www.rsc.org/

R. -Z. Li,[ac] Rui Peng,[b] K. D. Kihm,[a] S. Bai,[f] D. Bridges,[a] U. Tumuluri,[b] Z. Wu,[b] T. Zhang,*[c] G. Compagnini,[d] Z. Feng,[e] and A. Hu*[af]

Direct laser-reduction of graphene oxide (GO), as a lithography-free approach, has been proven effective in manufacturing in-plane micro-supercapacitors (MSCs) with fast ion diffusion. However, the power density and charge/discharge rate are still limited by the relatively low conductivity of electrodes. Here, we report a facile approach by exploiting femtolaser in-situ reduction of hydrated GO and chloroauric acid ($HAuCl_4$) nanocomposite simultaneously, which incorporates both the patterning of rGO electrodes and the fabrication of Au current collectors in a single step. These flexible MSCs boast achievements of one hundred fold increase in electrode conductivities up to 1.1×10^6 S/m, which provide superior rate capability (50% for the charging rate increase from 0.1 V/s to 100 V/s), sufficiently high frequency responses (362 Hz, 2.76 ms time constant), and large specific capacitance of 0.77 mF/cm^2 (17.2 F/cm^3 for volumetric capacitance) at 1 V/s, and 0.46 mF/cm^2 (10.2 F/cm^3) at 100 V/s. The use of photo paper substrates enables the flexibility of this fabrication protocol. Moreover, proof-of-concept 3D MSCs are demonstrated with enhanced areal capacitance (up to 3.84 mF/cm^2 at 1 V/s) while keeping high rate capabilities. This prototype of all solid-state MSCs demonstrates the broad range of potentials of thin-film based energy storage device applications for flexible, portable, and wearable electronic devices that require a fast charge/discharge rate and high power density.

Introduction

Recent developments in portable electronics have shown an increased demand for miniaturized energy-storage units as flexible chips with enhanced functionality and integration capabilities.[1-4] Notably, micro-supercapacitors (MSCs) are highly promising innovations for on-chip applications requiring a high spike of current as well as a high frequency response for alternating current (ac) line filtering.[3, 5-8] The capability of retaining high specific capacitance during ultrafast charging/discharging is essential for these high-performance supercapacitor application.[9] Furthermore, the use of electric double-layer micro-supercapacitors (EDL-MSCs) is preferred due to their rapid and reversible adsorption/desorption of ions at the electrolyte–electrode interface.[10, 11] In this regard, the EDL-MSCs require highly conducting electrodes with large accessible surface areas, and reduced graphene oxide (rGO) is regarded as a potentially excellent material for these EDL-MSC electrodes.[2, 4, 12, 13]

Planar rGO-MSCs significantly facilitate rapid ion transportation due to shorter ion diffusion pathways in comparison with those of conventional stacked supercapacitors.[4, 14] In these EDL rGO-MSCs, Au or Pt current collectors are used to further minimize internal resistance. However, the photolithography technology patterning of these rGO electrodes and wet etching process of Au/Pt current collectors[2, 4, 5, 7] limit the potential to integrate them into flexible substrates such as heat sensitive polymers and papers.[3]

[a] *Department of Mechanical, Aerospace, and Biomedical Engineering, University of Tennessee, Knoxville, 37996, United States E-mail: ahu3@utk.edu*
[b] *Center for Nanophase Materials Sciences and Chemical Science Division, Oak Ridge National Laboratory, P.O. Box 2008, Oak Ridge, 37831-6493, United States*
[c] *School of Electronic Science and Engineering, Southeast University, Key Laboratory of Micro-Inertial Instrument and Advanced Navigation Technology, Ministry of Education, Nanjing 210096, China*
[d] *Dipartmento di Scienze Chimiche, Università di Catania, Viale A. Doria 6, Catania 95125, Italy*
[e] *Materials Processing and Joining, Materials Science and Technology Division Oak Ridge National Laboratory, P.O. Box 2008, Oak Ridge, TN 37831-6083, United States*
[f] *Institute of Laser Engineering, Beijing University of Technology, 100 Pingle Yuan, Chaoyang District, Beijing 100124, China*

† Electronic Supplementary Information (ESI) available: XRD and high resolution XPS, bending performances, cycle life, five supplementary notes on calculation of the specific capacitance, comparison mechanism of FS and CW lasers, FS enhanced reduction of rGO/Au nanocomposites, mechanical flexibility of rGO/Au FS MSCs, and electrochemistry performance of rGO/Au MSCs with different concentration of $HAuCl_4$, respectively. See DOI: 10.1039/x0xx00000x

Gao et al.[10] described the direct writing of planar rGO MSCs through laser reduction and patterning hydrated GO films. Although the device suffered from a low charge/discharge rate due to its high internal resistance, laser writing technology is a flexible and simplified method for MSC fabrication. El-Kady et al,[15] later reported laser scribed rGO-MSCs using a LightScribe DVD optical drive, and demonstrated that the restacking and agglomeration of graphene sheets are suppressed through laser reduction. Furthermore, the laser-written interdigitated MSCs displayed enhanced charge-storage capacity.[3] These pioneering works paved a way toward the massive production of rGO-MSCs. Nevertheless, mainly due to the absence of highly conductive current collectors and as well as to the relatively low conductivity of laser script graphene (LSG) electrodes, the rate capability of LSG-MSC is still limited. Meanwhile, the time constant (19 ms)[3] corresponding to the frequency response of LSG-MSCs is much longer than that of conventional fabricated MSCs such as graphene/CNT composite-based MSCs (4.8 ms)[7] or plasma-reduced graphene MSCs (0.28 ms).[4] Thus, more innovative laser direct writing protocols are needed to develop highly conductive electrodes and current collectors.

From a substrates perspective, cellulose-based paper holds great promise as a biodegradable substrate for flexible electronics because of its low-cost, disposable, flexible, ultra-thin and light,[16, 17] with a vast demonstration of antennas,[18] sensors,[19-23] microfluidics,[24] transistors,[25-27] solar cells,[28, 29] memory devices[30] and batteries[31-34]. This and similar devices reveal a trend towards incorporating differing sensors and electronic components onto a single paper substrate to produce high-density integrated systems,[19] coupled with paper based supercapacitors are desirable. Nevertheless, except for several examples [23, 35, 36] in a stacked structure, no study focuses high rate MSCs on papers targeting aforementioned applications, and potentially substitute conventional aluminium capacitors for paper electronics.

Herein, we report a facile approach by exploiting laser in-situ reduction of hydrated GO and chloroauric acid ($HAuCl_4$) nanocomposite simultaneously, which incorporates both the patterning of rGO electrodes and the fabrication of Au current collectors in a single step. The main objective of this innovative fabrication of EDL-MSCs is to develop highly conductive electrodes that allow high rate capability and fast frequency response. Also, prove of concept 3D MSCs are demonstrated with multifold increase of areal capacitance to fully utilize the limited space available for on chip energy storage. Unlike the continuous wave (CW) lasers, the use of femtosecond (FS) lasers provide excellent device performance by utilizing multiphoton polymerization,[37, 38] reduction,[39-41] melting[42, 43] and etching.[43] The strong peak power of ultrashort pulses enables a nonlinear multiphoton interaction with the materials within the focal point, and leads to the following advantages: 1) high conductivity of rGO,[44] improving rate capability, 2) porous structures of rGO with enhanced accessible surface area,[12, 45, 46] increasing specific capacitance and 3) minimization of linewidth to a few micrometer or even sub-micrometer scale, facilitating the integration with on-chip devices.[47-49] Finally, the fabrication of MSCs on paper enables all paper-based systems that can work independently and sustainably.[50] Thereby, an additional merit of the present femtolaser-written EDL-MSCs is the ability to use cellulose-based paper substrates that are biodegradable and compatible with flexible electronics.

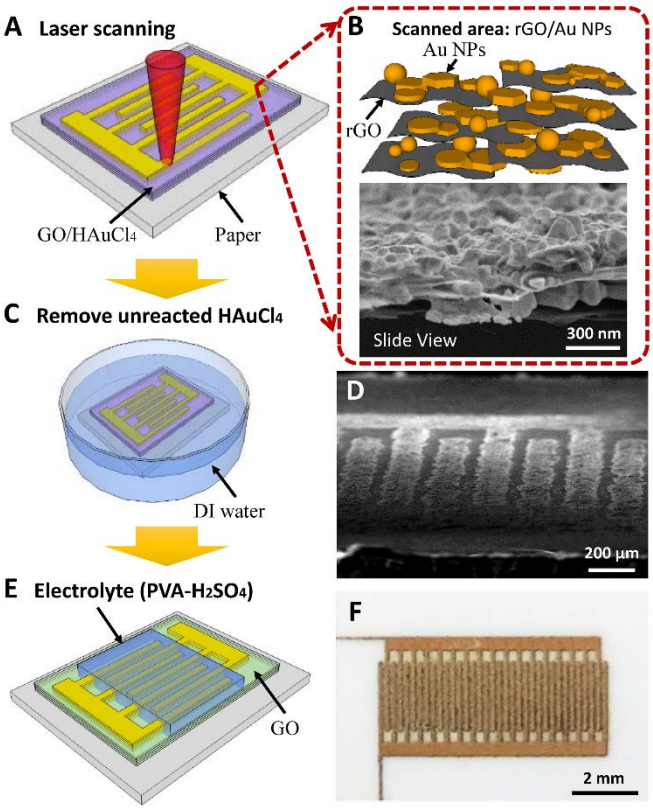

Fig. 1 Schematic illustration and photos of rGO/Au-MSCs (Micro-supercapacitors) fabrication onto a paper substrate. The fabrication process includes: A) direct FS laser writing of rGO/Au microelectrodes, B) the SEM image of rGO/Au microelectrodes, C) removal of unreacted $HAuCl_4$ by rinsing in DI water, D) SEM image of the interdigitated rGO/Au microelectrodes, E) spreading PVA/H_2SO_4 electrolyte onto the microelectrodes, and F) the optical image of the final rGO/Au FS-MSC.

Experimental sections

All reagents used in the experiments were purchased from Fisher Scientific and used without further purification. The photo paper was purchased from Home Depot®.

Fabrication of MSCs on Paper

The fabrication process is conclude in Fig. 1 including following steps: applying GO/$HAuCl_4$ mixture onto photo paper, direct laser writing of rGO/Au electrodes, removal of unreacted $HAuCl_4$ and applying solid state electrolyte.

Aqueous dispersion of GO was fabricated from natural graphite flakes using a modified Hummers method, the details of which are described elsewhere.[51] GO/$HAuCl_4$ mixture was prepared by dissolving 0.375 mM gold chloride ($HAuCl_4$) into a 1 mL GO suspension (7.5 mg mL^{-1}). Then, the GO/$HAuCl_4$ mixture was spread onto a photo paper with an area density of 50 µL cm^{-2} and left at room temperature for several hours to dry.

Direct laser writing was conducted by a femtosecond fiber laser (Model: Cazadero, Calmar Laser Inc.) with 1030 nm central wavelength, and 400 fs pulse duration at a repetition rate of 120 kHz. Also, a CW laser (Verdi G5, Coherent) with 532 nm wavelength was used for laser writing to perform a comparative study. The laser beam was introduced into an upright microscope system and focused with a long working-distance 20x objective lens (LMPlan, NA0.40, Amscope). A computer-controlled 2-axis motorized platform moved the MSC samples at a typical writing speed of 1 mm s^{-1} with a typical 80 mW laser power. The MSC contains interdigitated electrodes of approximately 140 µm in width with 60 µm spacing, conforming to a single cell dimension of 6.9 mm in length and 1.9 mm in width. The area of a single cell is 0.1311 cm^2.

Laser written samples were rinsed with deionized water several times to remove unreacted $HAuCl_4$ and left to dry at room temperature. A similar process was used to prepare rGO microelectrodes from GO aqueous dispersion (7.5 mg mL^{-1}) without $HAuCl_4$.

The H_2SO_4/PVA hydrogel electrolyte was prepared following the procedure as previously reported.[4] A thin layer of H_2SO_4/PVA hydrogel electrolyte was drop-casted onto the laser-written microelectrodes (10 µL cm^{-2}), which were left at room temperature overnight to ensure that the electrolyte completely diffused into the microelectrodes.

Characterization

The morphology and microstructures were characterized by a dual beam FIB/SEM instrument (Zeiss Auriga). Also, TEM and HRTEM observations were performed using a ZEISS LIBRA 200. Raman spectra were measured by a micro-Raman spectrometer using a laser excitation at 532 nm (Planar RAM-S Micro Raman System, Planartech, LLC). XPS analysis was performed using a PHI 5000 Versa Probe spectrometer (ULVAC-PHI, Japan) equipped with a monochromatic Al-Ka (1486.6 eV). X-ray source and an analyzer pass energy of 280 eV (55 eV for High-resolution XPS spectra). The electrode conductivities were determined from $\sigma = l/(twR)$,[52, 53] where the resistance R was measured by a digital voltmeter (HP 3456A), and t, w and l are the electrode thickness, width, and length, respectively.

The electrochemical performances of the MSCs were examined by conducting a CV test, GCD test and EIS test using an electrochemical workstation (SP-200, Bio-Logic Science Instruments). Both CV and GCD tests were conducted using a two-electrode setup, while the EIS test was conducted over a frequency range from 0.1 Hz to 1 MHz with an amplitude of 10 mV at the open-circuit potential. Calculations of the specific capacitance are discussed in detail in Supplementary Note 1 (ESI).

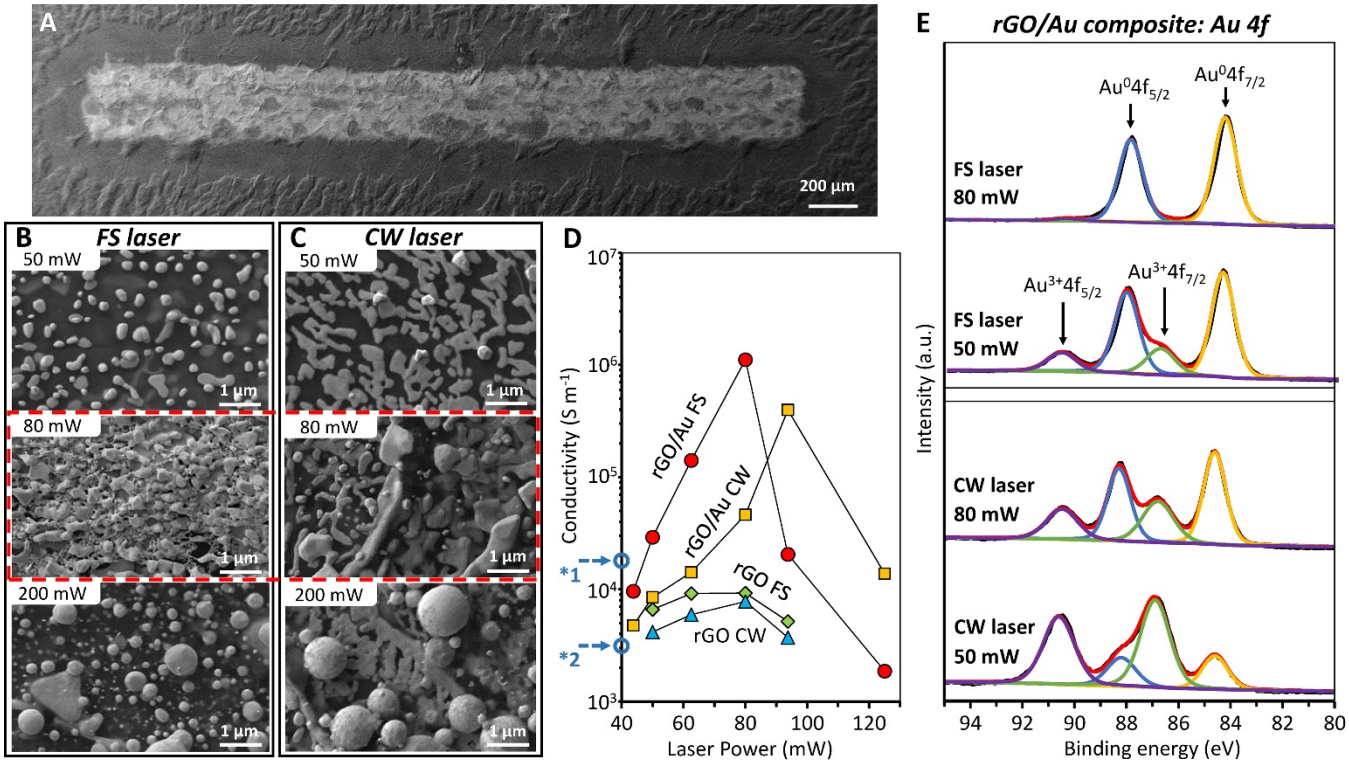

Fig. 2 Laser-written electrodes: A) SEM image of FS (femtosecond) laser-written rGO/Au microelectrodes, B) SEM images of the FS laser (1030 nm, 400 fs pulse duration)-written rGO/Au microelectrodes with average laser power of 50 mW, 80mW and 200 mW, c) SEM images of the FS laser (532 nm)-written rGO/Au microelectrodes with average laser power of 50 mW, 80mW, and 200 mW, D) conductivity of both the rGO/Au microelectrodes and rGO microelectrodes (markings *1 and *2 denote the reported conductivities for FS laser-reduced rGO[23] and infrared CW laser-reduced rGO[15], respectively), and E) XPS-fitted Au 4f core peaks for both the FS- and CW- rGO/Au microelectrodes.

Results and discussion

Femtolaser beam irradiation onto a gel layer of $HAuCl_4$ with GO sheets on a glossy photo paper substrate reduces $HAuCl_4$ to Au

nanoparticles (NPs) and GO to rGO (Fig. 1A). Detailed XRD and XPS spectra also confirmed the conversion of GO into rGO (Fig. S1, ESI). This FS laser writing creates a stacked-structure, with Au NPs of an average size of 150 nm attached to both sides of the rGO flakes, which are on the order of a few microns (Fig. 1B). These Au NPs act as nano-spacers between rGO sheets to constitute the rGO/Au microelectrode. More importantly, these Au NPs serve as highly conducting pathways[54] after sintering and significantly reduce the resistance of EDL-MSC electrodes. The constructed rGO/Au microelectrodes are immersed in deionized (DI) water to remove unreduced $HAuCl_4$ (Fig. 1C and 1D). Finally, the microelectrodes are coated with a thin layer of sulfuric acid/polyvinyl alcohol (H_2SO_4/PVA) hydrogel in order to conform to a solid state EDL-MSC (Fig. 1E and 1F).

Laser-written rGO/Au Electrodes

The detailed investigations of laser scripted rGO/Au electrodes as a function of laser power are shown in Fig. 2. The brighter SEM image intensity of the laser scanned area in Fig. 2A is attributed to the reduced Au NPs that emit abundant secondary electrons. Further magnified images show detailed definitions of Au NPs for the case of femtolaser at 1030 nm with a pulse duration of 400 fs (Fig. 2B) and for the case of comparative continue wave laser scanning at 532 nm (Fig. 2C). The gel layer of GO/$HAuCl_4$ is being reduced to rGO/Au (50 mW average laser power), the increase in laser power leads to the growth and sintering of Au NPs (80 mW), and further increased laser power transforms Au NPs into congregated Au spheres (200 mW).

Given the identical average laser power of 80 mW (as the red dash line marked in Fig. 2.), the prevailing photothermal effects of the CW laser generates sufficient heat energy to melt Au NPs, thus forming relatively discrete Au NPs, whereas the less prevailing photothermal energy of the FS laser forms continuous Au NPs membrane due to the multi-photon absorption mechanism (see Supplementary Note 2, ESI). The reduction mechanism of an FS laser is elucidated in two stages; multi-photon reduction prevails under the laser power slightly above the threshold (44 mW in this work), whereas photothermal reduction, sintering and melting dominate at a higher laser power.

Note that in our experiment no additional reducing agent was added. Hence, the thermal reducing of $AuCl_4^-$ can be attributed to a reductive deposition of Au^0 reduced by laser reduced rGO sheets (or GO sheets)[55] as well as the thermal decomposition of $HAuCl_4$.[56]

Firstly, the mechanism of this reductive deposition process likely involves Galvanic displacement[57, 58] and redox reaction by relative potential difference.[55, 59] When $AuCl_3$ ($HAuCl_4 \cdot 4H_2O$, i.e. $AuCl_3 \cdot HCl \cdot 4H_2O$ in this work) is dissolved in a solvent, different ionic conformation can be formed depending on the amount of the coordinating agent.[60] Water (in this work) or acetonitrile preferentially leads to a square planar geometry of $AuCl_4^-$.[60] The reduction potential of the rGO (+0.38 V *vs.* SHE, standard hydrogen electrode) is much below as compared to that of $AuCl_4^-$ (+1.002 V *vs.* SHE).[59, 61] Therefore, gold cations (Au^{3+}) in a salt solution can be reduced spontaneously, because of the electrons donated from negative-charged rGO sheets and the lower reduction potential of rGO.[59] For the case that water is used as the solvent, it is understood that the direct reduction from Au^{3+} to Au^0 takes place:[62]

$$AuCl_4^- + 3e \rightarrow Au^0\downarrow + 4Cl^- \quad (1)$$

This is consistent with the X-ray photoelectron spectra (XPS) which will be discussed afterwards. Similar mechanism was proposed to explain the decoration of carbon nanotubes with metal particles.[63]

Additionally, the $AuCl_4^-$ also can be directly reduced by GO sheets, which are composed of many small aromatic conjugated domains modified with the oxygen-containing functional groups. These aromatic conjugated domains act as electron-donating sources to reduce Au^{3+} and form tiny Au NPs.[64] After adding of $HAuCl_4 \cdot 4H_2O$ into GO aqueous dispersion, this reaction is confirmed by the SEM image (Fig. S2A, ESI) with a few tiny Au NPs formed on GO sheets with average size of 20 nm and the XRD pattern (Fig. S2B, ESI).

Secondly, the laser irradiation creates strong photothermal effect which not only promotes aforementioned reaction, and also leads to the decomposition of $AuCl_4^-$:[56]

$$HAuCl_4 \rightarrow HCl + AuCl_3 \quad (2)$$

$$AuCl_3 \rightarrow Au + AuCl + Cl_2\ (> 160\ ^\circ C) \quad (3)$$

$$2AuCl \rightarrow 2Au + Cl_2\ (> 289\ ^\circ C) \quad (4)$$

This process consequently converts $AuCl_4^-$ to Au NPs at aforementioned high laser power.

The rGO/Au microelectrodes show dramatically enhanced in-plane conductivities up to two order-of-magnitudes larger than the rGO electrodes or as high as 1.1×10^6 S m^{-1}, which depicts the pronounced contributions of Au NPs to the enhancement of conductivity (Fig. 2D). The synergic effect of highly conductive Au NP membranes and bridge-connected rGO sheets with sintered Au NPs significantly increases the microelectrode conductivities. This highly conductive rGO/Au microelectrode reduces the internal resistance of EDL-MSC and promotes its charge/discharge rate capabilities. In contrast, a very low conductivity of 7.7×10^{-3} S m^{-1} is measured for the non-scanned area of GO that serves as a separator, which is consistent with that of the previously reported hydrated GO.[10]

The conductivity of rGO/Au microelectrode increases with increasing laser power until it reaches a peak value and quickly decreases thereafter, as the bridge-connections of rGO sheets are weakened by laser ablation that separately distributes Au NPs (Fig. 2B and 2C) and breaks the conductive pathways. The substantially higher peak power of the pulsed FS laser is more aggressively damaging to the rGO/Au microelectrodes than the CW laser. This explains the reason for the maximum conductivity peak occurring at a lower laser power for the FS laser than CW laser (Fig. 2D). Also, SEM imaging clearly identifies the damaged area of the rGO/Au FS microelectrode (Fig. S3, ESI).

Additionally, the higher conductivity of rGO/Au FS in comparison to that of rGO/Au CW is mainly due to the enhanced reduction of gold from $HAuCl_4$ by FS laser writing as the X-ray photoelectron spectra (XPS) show in Fig. 2F. Both $Au^0 4f^{5/2}$ (88.3 eV) and $Au^0 4f^{7/2}$ (84.2 eV) peaks represent the binding energies of reduced Au NPs, whereas the minor peaks at higher binding energy (90.5 eV and 86.8 eV, respectively), represent Au ions adsorbed on the composite surface.[63, 65] The Au^0 doublet peak intensities increase with increasing laser power. Furthermore, the FS laser more efficiently reduces $HAuCl_4$ to Au NPs showing much lower Au ion peaks in comparison with the CW laser. Meanwhile, femotolaser-

enhanced reduction of GO sheets with a higher C/O ratio of 12.57 in rGO/Au FS microelectrodes may also contribute to the higher conductivity of rGO-Au microelectrodes (Supplementary Note 3, ESI). Another factor, as aforementioned, that the more continues Au NPs membrane written by FS laser at a laser power of 80 mW provides more highly conductive pathways, which may response for the higher conductivity peak value of rGO/Au FS microelectrodes as well.

Note that, the FS laser scanning creates abundant nano-porous holes that increase the accessible surface areas and EDL-MSC capacitance (Fig. 3A and 3B). This is consistent with Raman spectra shown in Fig. 3C for the case of 80 mW laser power scanning. The reduction of GO sheets into rGO increases the Raman peak ratio of I_D/I_G from 0.91 to 0.94 (CW) or 1.03 (FS), which shows that FS laser reduction results in more structural changes and defects associated

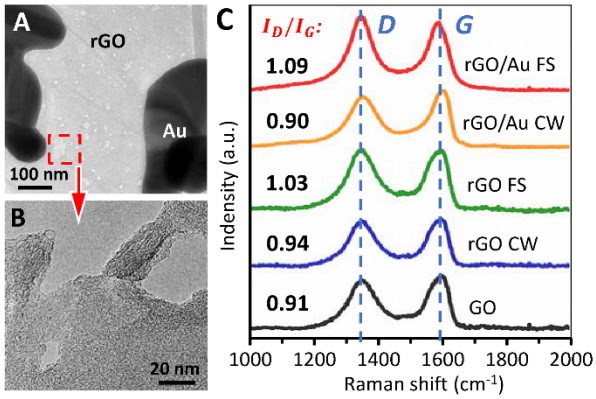

Fig. 4 Nano-porous structures of FS laser-written rGO/Au microelectrodes at a laser power of 80 mW: A) TEM and B) HRTEM images of the FS laser-written rGO/Au microelectrodes, showing the nano-porous structures, and C) Raman spectra of GO sheet (black curve), rGO microelectrodes (blue for CW and green for FS), and rGO/Au microelectrodes (orange for CW and red for FS).

with increased nanoporous edges than CW laser reduction. This observation is conserved when Au NPs are reduced from $HAuCl_4$, showing an I_D/I_G increase to 0.90 and 1.09 for CW and FS lasers, respectively.

Electrochemical Characterization of Laser-Written MSCs

To improve the charge/discharge rate capabilities of MSCs, a low equivalent series resistance (ESR) is required.[4] Considering the morphological and electrical characteristics of FS laser written rGO/Au microelectrodes, therefore, the laser power of 80 mW was employed to provide the highest conductivity of microelectrodes to minimize ESR.[66]

Cyclic voltammetry (CV) experiments (Fig. 4A and 4B) for the electrochemical performance evaluation of laser-written MSCs show that the rGO/Au FS-MSCs provide a fast charge transfer with a sufficiently low ESR, which is evidenced by retaining a quasi-rectangular CV curve for up to the scan rate of 100 V s^{-1}.[4, 67] In the absence of Au NPs, despite of the quasi-rectangular shaped CV curves are observed at a scan rate of 1 V s^{-1}, the area of rGO-FS CV curve, which implies specific capacitance, diminishes to zero because of the enlarged ESR without any bridge-connections of rGO sheets by Au NPs; and thus, the CV curve collapses into a line at 100 V s^{-1}.[7] Meanwhile, the narrower CV curves for the CW laser-written MSCs are mainly due to their relatively larger ESRs. This discrepancy is more pronounced with an increasing scan rate.[12]

The galvanostatic charge/discharge (GCD) curves for rGO/Au FS (Fig. 4C) show nearly symmetrical triangle-shaped curves as an ideal EDL-MSC with no apparent internal resistance (*iR*) drop. The slight non-linearity in the curves implies a charge–transfer phenomena that can be ascribed to the reaction of oxygen contained in the

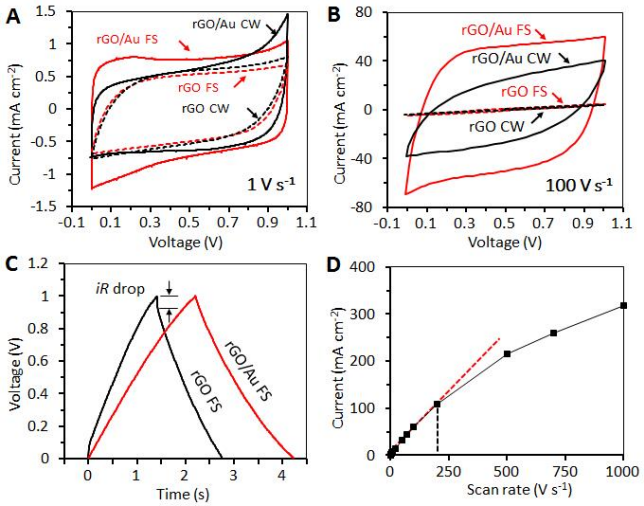

Fig. 3 Comparison of electrochemical performances of both the laser-written rGO/Au-MSCs and rGO-MSCs: A,B) cyclic voltammetry (CV) curves obtained at a scan rate of 1 V s^{-1} and 100 V s^{-1}, respectively, C) galvanostatic charge/discharge (GCD) curves measured at a scan rate of 50 μA (381 μA cm^{-2}) for rGO/Au FS-MSCs and rGO FS-MSCs, D) the discharge current of rGO/Au FS-MSCs as a function of the scan rate.

surface functional groups of rGO sheets.[52] For rGO FS without Au NPs, however, the curves show a notable *iR* drop of about 0.1 V, which confirms a relatively larger ESR.[3, 52] For rGO/Au FS, the linear dependence of the discharge current density for the scan rate up to 200 V s^{-1} (Fig. 4D) further demonstrates that the use of Au NPs significantly enhances the power output capabilities of MSCs.

As the current collector, the Au NPs contribute to remarkably enhancing the areal capacitance at high scan rates for rGO/Au FS-MSCs as well as rGO/Au CW-MSCs (Fig. 5A) due to the reducing of ESR, while the EDL capacitance contributed by bare in-plane Au microelectrodes is very low (typically <0.01 mF cm^{-2} at a scan rate of 1 V s^{-1} and <0.001 mF cm^{-2} at a scan rate of 100 V s^{-1}).[4] Therefore, the EDL capacitance of rGO/Au MSCs mainly comes from the ion absorption and desorption on rGO sheets surface, which is also evidenced by the areal capacitance close to 2 mF cm^{-1} at a low scan rate of 0.1 V s^{-1}. Meanwhile, the nanoporous structures introduced by FS laser may contribute to enhance the specific capacitance of the FS laser-written MSCs at all scan rates due to the enlarged accessible area of rGO sheets.

The areal capacitance at 1 V s^{-1} of rGO/Au FS-MSCs is superior to the other three tested MSCs (the inset graph in Fig. 5A); however, this superiority is dramatically more pronounced at a higher scan rate. At 100 V s^{-1}, for example, the areal capacitances of both rGO/Au FS-MSCs (0.46 mF cm^{-2}) and rGO/Au CW-MSCs (0.20 mF cm^{-2}) are over 100 times larger than those of the rGO based MSCs without Au NPs. At 1000 V s^{-1}, at which a smaller drop of areal

capacitance is crucial to ensure the rate capability, the rGO/Au FS-MSCs provide a high areal capacitance of 95 μF cm^{-2}, which is about 20 times higher than the previously reported areal capacitance for MSCs using a plasma-reduced graphene oxide (4.5 μF cm^{-2})[4] and over 5 times higher than laser-written porous carbon MSCs (<20 μF cm^{-2}).[52]

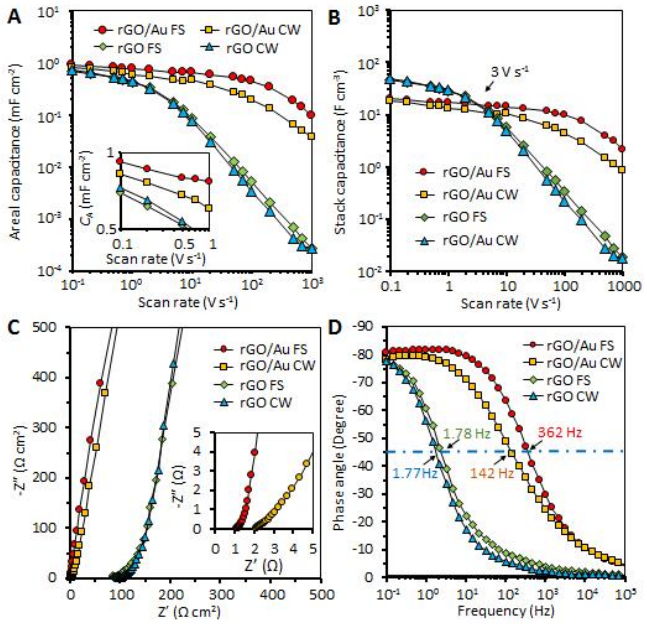

Fig. 5 Comparison of electrochemical performances of both the laser-written rGO/Au-MSCs and rGO-MSCs: A) areal capacitance C_A as a function of the scan rate (inset shows a magnified low-scan-rate region), B) stack capacitance C_s as a function of the scan rate, C) the Nyquist plot of the impedance of the MSCs (inset shows a magnified high-frequency region), and D) the Bode plot of impedance of the MSCs.

From volumetric perspective (Fig. 5B), the stacked capacitances of rGO/Au MSCs written by both FS laser and CW laser are remarkably higher than that of rGO MSCs without Au NPs at a scan rate from 3 V s^{-1} to 1000 V s^{-1}, which is consistent with the areal capacitance. For example, at 100 V s^{-1}, the stacked capacitance of rGO/Au FS-MSCs (10.2 F cm^{-3}) is more than 30 times larger than those of the rGO based MSCs without Au NPs. At low scan rates below 3 V s^{-1}, the stacked capacitance of rGO MSCs without Au NPs (~50 F cm^{-3}) is still remarkably higher than that of rGO/Au MSCs (~18 F cm^{-3}), which is due to the thinner rGO microelectrodes without Au NPs than the rGO/Au microelectrodes. Nevertheless, the stacked capacitance of rGO/Au MSCs is still over 8 times larger than those previous reported laser-scripted MSCs (<2.5 F cm^{-3}).

Note that the rGO/Au FS-MSC exhibits remarkably enhanced rate capabilities, for example, retaining 71% of its capacitance when the charging rate is increased from 0.1 V s^{-1} to 10 V s^{-1} and 50% for the increase from 0.1 V s^{-1} to 100 V s^{-1}. These enhanced rate capabilities of the rGO/Au FS-MSC are attributed to the remarkably high specific capacitance at high scan rates.

Electrochemical impedance spectroscopy (EIS) provides a consistent insight for the superior performance of rGO/Au FS-MSCs as shown in the Nyquist plot of resistance (Z') vs capacitance (Z") (Fig. 5C). The high frequency region (the inset graph) shows small charge resistance for both the rGO/Au and rGO based MSCs and the steep Nyquist curves imply the short ion diffusion pathway and fast ion diffusion for such in-plane interdigitated geometry.[4] The ESR, which is equivalent to the intersection point with the Z'-axis, is determined to be 1.1 Ω cm^2 for rGO/Au FS-MSCs and 2.1 Ω cm^2 for rGO/Au CW-MSCs. Note that these ESR values are on the order of 1% of those for the rGO based MSCs with no Au NPs-bridged rGO sheets, namely, 91.2 Ω cm^2 for rGO-FS and 103.6 Ω cm^2 for rGO-CW. Furthermore, the high characteristic frequency f = 362 Hz (corresponding time constant $\tau = 1/f$ = 2.76 ms) at -45° phase angle[4] for rGO/Au FS-MSCs (Fig. 5D) turns out to be significantly higher than those for rGO/Au CW-MSCs (142 Hz), rGO FS-MSCs (1.78 Hz) and rGO CW-MSCs (1.77 Hz). This high frequency satisfies the requirement of the *ac* line fliting (larger than 120 Hz).

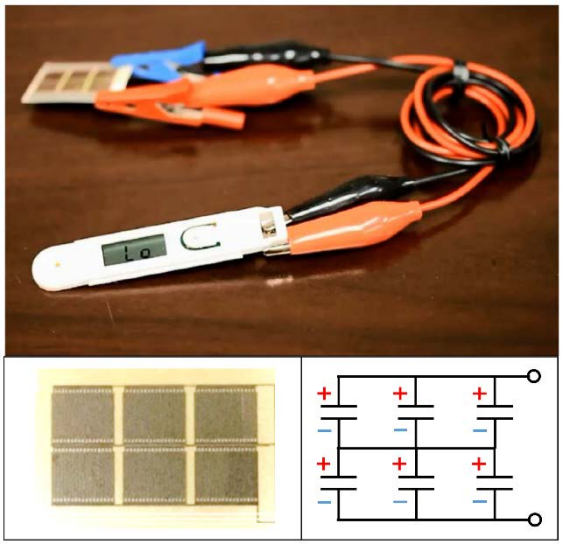

Fig. 6 A liquid crystal display (LCD) powered by an array of 6 rGO/Au FS-MSCs (the inset images show the actual rGO/Au FS-MSC array and its circuit diagram).

In addition, the rGO/Au FS MSCs shows the features of large-area good mechanical flexibility (Supplementary Note 4, ESI) and the excellent cycle life (Fig. S4, ESI). The capacitance decays only a mere 1% from the initial specific capacitance after 10,000 repeated charge/discharge cycles at a scan rate of 50 V s^{-1}, and 19.7% from the initial specific capacitance at a scan rate of 1 V s^{-1}. As a demonstration, Fig. 6 shows that a liquid crystal display (LCD) is powered by a rGO/Au FS array of 6 MSCs (see Video S1).

Demonstration of three dimensional (3D) rGO/Au FS MSCs

3D designs based on micro- and nano-structured architectures could potentially boost the areal energy density by fully utilizing the limited space available for on chip energy storage.[68] To date, such architectures have been produced in planar and 3D devices by conventional lithography,[69] nozzle printing,[68] and colloidal templating methods,[70] respectively, whereas no work has been reported about the 3D MSCs fabricated by laser writing.

Here, proof-of-concept 3D rGO/Au FS MSCs are demonstrated in Fig. 7 using a layer-by-layer drop-casting/laser-writing process. It is

well known that the laser power penetrating through the GO/$HAuCl_4$ film possesses an exponential decay along the depth[71] owing to the absorption of the GO/$HAuCl_4$ gel layer. On the other hand, the produced rGO and Au NPs can further prevent from a deep laser penetrating due to the strong surface plasmon resonance (SPR).[72, 73] As a result, the maximum thickness of surface reduced electrode is limited to about 500 nm because a thicker electrode would fall off from the substrate when immersed into DI water for washing. The weak bonding is caused by re-dispersion of unreacted GO sandwiched between the electrodes and paper substrate. However, if the deposition is controlled as the thickness of no more than 500 nm, a layer-by-layer assembly via repeating the drop-casting and laser reduction processes is practical to construct a 3D electrode.

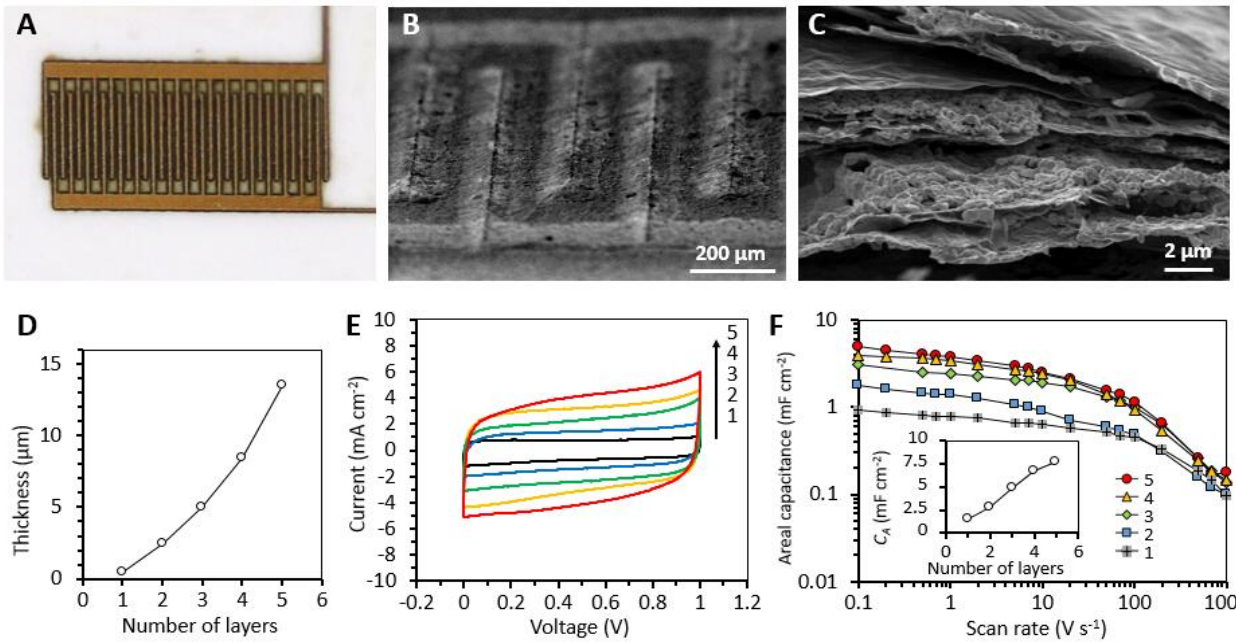

Fig. 7 3D rGO/Au-MSCs (Micro-supercapacitors) fabricated on a paper substrate: A) the optical image of a 5-layer 3D rGO/Au FS-MSC, B) the SEM image of the interdigitated 5-layer 3D rGO/Au microelectrodes, C) the cross-sectional view of a 5-layer 3D rGO/Au microelectrode, D) the maximum thickness of rGO/Au microelectrodes as a function of layer number, E) cyclic voltammetry (CV) curves obtained at a scan rate of 1 V s^{-1} with an increasing number of layers (marked by the black arrow), and F) areal capacitance C_A as a function of the scan rate (inset shows areal capacitance C_A as a function of the number of layers).

The photograph in Fig. 7A shows a laser-written 3D rGO/Au FS MSC, with a triangle shaped cross-sectional structure of microelectrodes (Fig. 7B). A typical SEM image in Fig. 7C clearly shows a multi-layer stacked cross-sectional structure of a 5-layer electrode with abundant micro-cavities between each layer. These cavities enlarge the interspace between rGO/Au micro-membranes to several micrometer scale. Nevertheless, few micro-cavities was observed for a single-layer microelectrode (Fig. 1B).

It is reasonable to expect that these micro-cavities are formed due to the release of gas during the reduction of GO and the coalescence of Au NPs, with an observation of multi-bubble generations (Fig. S5, ESI) with grayish smoke during laser writing. This diversity between a single-layer microelectrode and a multi-layer microelectrode probably due to the difference of gas release path during the laser writhing. Taking the fabrication of a 2-layer microelectrode for example, when laser writing the first layer, the produced gas directly release from the GO/$HAuCl_4$ gel. For the second layer case, non-neglectful amount of GO/$HAuCl_4$ gel is absorbed in the porous first-layer microelectrodes. During the laser writing, gas which produced from GO/$HAuCl_4$ gel creases bubbles inside the first-layer microelectrodes, or between the first and second-layer microelectrodes. The bubbles grow and push the surrounding rGO/Au membranes and creates micro-cavities, which multiply the thickness. This cavity-formation process is probably similar to that of the laser-fabricated micro-cavities inside PMMA slides.[42] As a result, the thickness of a single-layer microelectrode is around 0.45 µm, whereas it suddenly increase to 2.5 µm for a 2-layer microelectrode. A near-linear number of layers dependence of the maximum thickness is observed for microelectrodes over 2 layers, with approximate 13.7 µm in the central thickness for a 5-layer microelectrode (Fig. 7D).

Meanwhile, the triangle shaped cross-sectional structure can be attributed to the Gaussian intensity profile of the focused laser beam, of which the light intensity at the central area is significantly higher than the surroundings. The larger micro-cavities and fused Au NPs are preferably formed at the central area due to a higher reduction, leading to a thicker rGO/Au membrane.

These 3D rGO/Au FS MSCs keep a quasi-rectangular shaped CV curves and linear increase of current density with an increasing number of layers as shown in Fig. 7E. This is consistent with the near-linear number of layers dependence of areal capacitance as shown in the inset of Fig. 7F.

Noteworthy, high rate capabilities are largely maintained (Fig. 7F and 7G) by comparing the 3D multi-layer MSCs to a 2D single-layer

MSC. The 5-layer rGO F-MSC, for example, retaining 49% of its capacitance when the charging rate is increased from 0.1 V s^{-1} to 10 V s^{-1} and 23% for the increase from 0.1 V s^{-1} to 100 V s^{-1}. Correspondingly, the specific capacitances are 4.92 mF cm^{-2} at 0.1 V s^{-1}, 2.39 mF cm^{-2} at 10 V s^{-1}, and 1.12 mF cm^{-2} at 100 V s^{-1}, respectively. These values are comparable with that of those previous reported high-rate MSCs (the best capacitance is 2.8 mF cm^{-2} for rGO/CNT composite MSCs at a rate of 50 V s^{-1}), allowing for the more compact design of on-chip devices.

Conclusions

In summary, we successfully demonstrated flexible in-plane high performance rGO/Au MSCs that are fabricated through in-situ femtolaser writing. Without the need of complicated multi-step photolithography processes, the femtolaser writing allows for the simultaneous and direct reduction of GO/$HAuCl_4$ composites into a combination of rGO electrodes and Au collectors (Au NPs). It is evident that fused Au nanoparticle in-plane network significantly increases the conductivity meanwhile the porous graphene enhancing the capacitance. These flexible MSCs boast achievements of two order-of-magnitude-increased electrode conductivities of 1.1×10^6 S m^{-1} due to the highly conductive pathways created by Au NPs, with short ion diffusion pathways due to the in-plane design, superior rate capabilities (71% and 50% of capacitance retention for the charging rate increase from 0.1 V s^{-1} to 10 V s^{-1} and to 100 V s^{-1}, respectively), sufficiently high frequency responses (362 Hz, 2.76 ms time constant), large specific capacitance (0.77 mF/cm^2 at 1 V s^{-1}), and outstanding cycle stability (10,000 cycles). Moreover, proof-of-concept 3D MSCs are demonstrated with enhanced areal capacitance (up to 4.92 mF cm^{-2} at 1 V/s) while keeping high rate capabilities, which allows for the more compact on-chip design. Such high performance rGO/Au-FS MSCs promote their applications for flexible, portable and wearable electronic devices that require fast charge/discharge rates and high power densities. Furthermore, these new femtolaser-written MSCs can be potentially integrated with other electronic devices such as solar cells, gas sensors, field-effect transistors, and chip-level display devices.

Acknowledgements

We appreciate the research initiative funding provided by the University of Tennessee as a new hire package to AH. Part of the work including the Raman and FTIR work was conducted at the Center for Nanophase Materials Sciences, which is a DOE Office of Science User Facility. This work is also in part supported by NSFC under grant number 51575016, 61307066, P. R. China; the Fundamental Research Funds for the Central Universities and Graduate Innovation Program of Jiangsu Province under grant number KYLX_0125; the Beijing Oversea High-Level Talent Project and a strategic research grant (KZ20141000500, B-type) of Beijing Natural Science Foundation; Foundation of Key Laboratory of Micro-Inertial Instrument and Advanced Navigation Technology, Ministry of Education, China under grant number 201204, a strategic research project (KZ40005001) of the Education Commission. Additional support is granted by the Nano-Material Technology Development Program (NRF-2013R1A1A2060720) through the National Research Foundation (NRF) of Korea. We also appreciate Dr. John R Dunlap for his assistance in TEM (JIAM Analytical Instrument Facilities, University of Tennessee at Knoxville).

Notes and references

1. J. Chmiola, C. Largeot, P.-L. Taberna, P. Simon and Y. Gogotsi, *Science*, 2010, **328**, 480-483.
2. Z. Niu, L. Zhang, L. Liu, B. Zhu, H. Dong and X. Chen, *Adv Mater*, 2013, **25**, 4035-4042.
3. M. F. El-Kady and R. B. Kaner, *Nature communications*, 2013, **4**, 1475.
4. Z. S. Wu, K. Parvez, X. Feng and K. Mullen, *Nature communications*, 2013, **4**, 2487.
5. D. Pech, M. Brunet, H. Durou, P. Huang, V. Mochalin, Y. Gogotsi, P. L. Taberna and P. Simon, *Nat Nanotechnol*, 2010, **5**, 651-654.
6. J. Lin, C. Zhang, Z. Yan, Y. Zhu, Z. Peng, R. H. Hauge, D. Natelson and J. M. Tour, *Nano Lett*, 2013, **13**, 72-78.
7. M. Beidaghi and C. Wang, *Adv Funct Mater*, 2012, **22**, 4501-4510.
8. M. Beidaghi and Y. Gogotsi, *Energy & Environmental Science*, 2014, **7**, 867-884.
9. G. Wang, H. Wang, X. Lu, Y. Ling, M. Yu, T. Zhai, Y. Tong and Y. Li, *Adv Mater*, 2014, **26**, 2676-2682, 2615.
10. W. Gao, N. Singh, L. Song, Z. Liu, A. L. Reddy, L. Ci, R. Vajtai, Q. Zhang, B. Wei and P. M. Ajayan, *Nature nanotechnology*, 2011, **6**, 496-500.
11. Y. Zhai, Y. Dou, D. Zhao, P. F. Fulvio, R. T. Mayes and S. Dai, *Adv Mater*, 2011, **23**, 4828-4850.
12. L. L. Zhang, X. Zhao, M. D. Stoller, Y. Zhu, H. Ji, S. Murali, Y. Wu, S. Perales, B. Clevenger and R. S. Ruoff, *Nano letters*, 2012, **12**, 1806-1812.
13. C. Zhang, W. Lv, Y. Tao and Q.-H. Yang, *Energy & Environmental Science*, 2015, **8**, 1390-1403.
14. J. J. Yoo, K. Balakrishnan, J. Huang, V. Meunier, B. G. Sumpter, A. Srivastava, M. Conway, A. L. Reddy, J. Yu, R. Vajtai and P. M. Ajayan, *Nano Lett*, 2011, **11**, 1423-1427.
15. M. F. El-Kady, V. Strong, S. Dubin and R. B. Kaner, *Science*, 2012, **335**, 1326-1330.
16. D. Tobjork and R. Osterbacka, *Adv Mater*, 2011, **23**, 1935-1961.
17. R. Z. Li, A. Hu, T. Zhang and K. D. Oakes, *ACS applied materials & interfaces*, 2014, **6**, 21721-21729.
18. A. Russo, B. Y. Ahn, J. J. Adams, E. B. Duoss, J. T. Bernhard and J. A. Lewis, *Advanced materials*, 2011, **23**, 3426-3430.
19. E. W. Nery and L. T. Kubota, *Anal Bioanal Chem*, 2013, **405**, 7573-7595.
20. Y. Wang, L. Ge, P. Wang, M. Yan, S. Ge, N. Li, J. Yu and J. Huang, *Lab Chip*, 2013, **13**, 3945-3955.
21. J. Wang, J. Jiu, M. Nogi, T. Sugahara, S. Nagao, H. Koga, P. He and K. Suganuma, *Nanoscale*, 2015, DOI: 10.1039/C4NR06494A.
22. D. D. Liana, B. Raguse, J. J. Gooding and E. Chow, *ACS applied materials & interfaces*, 2015.
23. L. Ge, P. Wang, S. Ge, N. Li, J. Yu, M. Yan and J. Huang, *Anal Chem*, 2013, **85**, 3961-3970.

24. R. Fobel, A. E. Kirby, A. H. Ng, R. R. Farnood and A. R. Wheeler, *Adv Mater*, 2014, **26**, 2838-2843.
25. U. Zschieschang, T. Yamamoto, K. Takimiya, H. Kuwabara, M. Ikeda, T. Sekitani, T. Someya and H. Klauk, *Advanced Materials*, 2011, **23**, 654-658.
26. J. Huang, H. Zhu, Y. Chen, C. Preston, K. Rohrbach, J. Cumings and L. Hu, *ACS Nano*, 2013, **7**, 2106-2113.
27. Y. Fujisaki, H. Koga, Y. Nakajima, M. Nakata, H. Tsuji, T. Yamamoto, T. Kurita, M. Nogi and N. Shimidzu, *Adv Funct Mater*, 2014, **24**, 1657-1663.
28. L. Leonat, M. S. White, E. D. Głowacki, M. C. Scharber, T. Zillger, J. Rühling, A. Hübler and N. S. Sariciftci, *The Journal of Physical Chemistry C*, 2014, **118**, 16813-16817.
29. M. C. Barr, J. A. Rowehl, R. R. Lunt, J. Xu, A. Wang, C. M. Boyce, S. G. Im, V. Bulovic and K. K. Gleason, *Adv Mater*, 2011, **23**, 3499-3505.
30. D. H. Lien, Z. K. Kao, T. H. Huang, Y. C. Liao, S. C. Lee and J. H. He, *ACS Nano*, 2014, **8**, 7613-7619.
31. L. Hu, H. Wu, F. La Mantia, Y. Yang and Y. Cui, *ACS Nano*, 2010, **4**, 5843-5848.
32. S. Leijonmarck, A. Cornell, G. Lindbergh and L. Wågberg, *Journal of Materials Chemistry A*, 2013, **1**, 4671-4677.
33. L. Nyholm, G. Nystrom, A. Mihranyan and M. Stromme, *Adv Mater*, 2011, **23**, 3751-3769.
34. G. Nyström, A. Razaq, M. Strømme, L. Nyholm and A. Mihranyan, *Nano letters*, 2009, **9**, 3635-3639.
35. L. Hu, H. Wu and Y. Cui, *Appl Phys Lett*, 2010, **96**, 183502.
36. X. Zhang, Z. Lin, B. Chen, S. Sharma, C.-p. Wong, W. Zhang and Y. Deng, *Journal of Materials Chemistry A*, 2013, **1**, 5835-5839.
37. Z. B. Sun, X. Z. Dong, W. Q. Chen, S. Nakanishi, X. M. Duan and S. Kawata, *Advanced Materials*, 2008, **20**, 914-919.
38. B. H. Cumpston, S. P. Ananthavel, S. Barlow, D. L. Dyer, J. E. Ehrlich, L. L. Erskine, A. A. Heikal, S. M. Kuebler, I.-Y. S. Lee and D. McCord-Maughon, *Nature*, 1999, **398**, 51-54.
39. T. Tanaka, A. Ishikawa and S. Kawata, *Appl Phys Lett*, 2006, **88**, 081107.
40. B.-B. Xu, L. Wang, Z.-C. Ma, R. Zhang, Q. Chen, C. Lv, B. Han, X.-Z. Xiao, X.-L. Zhang and Y.-L. Zhang, *ACS nano*, 2014.
41. Y. Y. Cao, N. Takeyasu, T. Tanaka, X. M. Duan and S. Kawata, *Small*, 2009, **5**, 1144-1148.
42. C. Zheng, A. Hu, K. D. Kihm, Q. Ma, R. Li, T. Chen and W. Duley, *Small*, 2015, **11**, 3007-3061.
43. Y. Bellouard and M.-O. Hongler, *Opt Express*, 2011, **19**, 6807-6821.
44. Y. Zhang, L. Guo, S. Wei, Y. He, H. Xia, Q. Chen, H.-B. Sun and F.-S. Xiao, *Nano Today*, 2010, **5**, 15-20.
45. P. Russo, A. Hu, G. Compagnini, W. W. Duley and N. Y. Zhou, *Nanoscale*, 2014, **6**, 2381-2389.
46. S. Han, D. Wu, S. Li, F. Zhang and X. Feng, *Adv Mater*, 2014, **26**, 849-864.
47. S. Shukla, X. Vidal, E. P. Furlani, M. T. Swihart, K.-T. Kim, Y.-K. Yoon, A. Urbas and P. N. Prasad, *Acs Nano*, 2011, **5**, 1947-1957.
48. S. Kawata, H.-B. Sun, T. Tanaka and K. Takada, *Nature*, 2001, **412**, 697-698.
49. B. B. Xu, H. Xia, L. G. Niu, Y. L. Zhang, K. Sun, Q. D. Chen, Y. Xu, Z. Q. Lv, Z. H. Li and H. Misawa, *Small*, 2010, **6**, 1762-1766.
50. L. Yuan, B. Yao, B. Hu, K. Huo, W. Chen and J. Zhou, *Energy & Environmental Science*, 2013, **6**, 470-476.
51. H. Wang, J. T. Robinson, X. Li and H. Dai, *J Am Chem Soc*, 2009, **131**, 9910-9911.
52. J. B. In, B. Hsia, J.-H. Yoo, S. Hyun, C. Carraro, R. Maboudian and C. P. Grigoropoulos, *Carbon*, 2015, **83**, 144-151.
53. R.-Z. Li, A. Hu, D. Bridges, T. Zhang, K. D. Oakes, R. Peng, U. Tumuluri, Z. Wu and Z. Feng, *Nanoscale*, 2015, **7**, 7368-7377.
54. R. Pasricha, S. Gupta and A. K. Srivastava, *Small*, 2009, **5**, 2253-2259.
55. K. K. Kim, A. Reina, Y. Shi, H. Park, L.-J. Li, Y. H. Lee and J. Kong, *Nanotechnology*, 2010, **21**, 285205.
56. S. M. Yoon, U. J. Kim, A. Benayad, I. H. Lee, H. Son, H. J. Shin, W. M. Choi, Y. H. Lee, Y. W. Jin, E. H. Lee, S. Y. Lee, J. Y. Choi and J. M. Kim, *ACS Nano*, 2011, **5**, 1353-1359.
57. L. A. Porter, H. C. Choi, A. E. Ribbe and J. M. Buriak, *Nano Letters*, 2002, **2**, 1067-1071.
58. J. Ou, C. Chang, Y. Sung, K. Ou, C. Tseng, H. Ling and M. Ger, *Colloids and Surfaces A: Physicochemical and Engineering Aspects*, 2007, **305**, 36-41.
59. B. S. Kong, J. Geng and H. T. Jung, *Chem Commun (Camb)*, 2009, DOI: 10.1039/b821920f, 2174-2176.
60. M. S. Abdou and S. Holdcroft, *Synthetic Met*, 1993, **60**, 93-96.
61. B. Raton, *Journal*, 2003.
62. H. C. Choi, M. Shim, S. Bangsaruntip and H. Dai, *J Am Chem Soc*, 2002, **124**, 9058-9059.
63. S. M. Kim, K. K. Kim, Y. W. Jo, M. H. Park, S. J. Chae, D. L. Duong, C. W. Yang, J. Kong and Y. H. Lee, *Acs Nano*, 2011, **5**, 1236-1242.
64. X. Zhou, X. Huang, X. Qi, S. Wu, C. Xue, F. Y. Boey, Q. Yan, P. Chen and H. Zhang, *The Journal of Physical Chemistry C*, 2009, **113**, 10842-10846.
65. A. Benayad, H.-J. Shin, H. K. Park, S.-M. Yoon, K. K. Kim, M. H. Jin, H.-K. Jeong, J. C. Lee, J.-Y. Choi and Y. H. Lee, *Chem Phys Lett*, 2009, **475**, 91-95.
66. W. Si, C. Yan, Y. Chen, S. Oswald, L. Han and O. G. Schmidt, *Energy & Environmental Science*, 2013, **6**, 3218-3223.
67. W.-W. Liu, Y.-Q. Feng, X.-B. Yan, J.-T. Chen and Q.-J. Xue, *Adv Funct Mater*, 2013, **23**, 4111-4122.
68. K. Sun, T. S. Wei, B. Y. Ahn, J. Y. Seo, S. J. Dillon and J. A. Lewis, *Advanced Materials*, 2013, **25**, 4539-4543.
69. S. R. Gowda, A. Leela Mohana Reddy, X. Zhan and P. M. Ajayan, *Nano Lett*, 2011, **11**, 3329-3333.
70. H. Zhang, X. Yu and P. V. Braun, *Nat Nanotechnol*, 2011, **6**, 277-281.
71. Y. Zhou, Q. Bao, B. Varghese, L. A. Tang, C. K. Tan, C. H. Sow and K. P. Loh, *Adv Mater*, 2010, **22**, 67-71.
72. D. K. Lim, A. Barhoumi, R. G. Wylie, G. Reznor, R. S. Langer and D. S. Kohane, *Nano Lett*, 2013, **13**, 4075-4079.
73. A. F. Zedan, S. Moussa, J. Terner, G. Atkinson and M. S. El-Shall, *ACS nano*, 2012, **7**, 627-636.